Microstructural features and thermal response of granulated Al and A356 alloy with relevant Sn additions

Paola Bassani [a], Matteo Molteni [b,*], Elisabetta Gariboldi [b]

[a] National Research Council of Italy, Institute of Condensed Matter Chemistry and Technologies for Energy, CNR-ICMATE, Via Previati 1/E, 23900 Lecco, Italy
[b] Politecnico di Milano, Department of Mechanical Engineering, Via La Masa 1, 20156 Milan, Italy

HIGHLIGHTS

- Al-Sn and A356-Sn composite Phase Change Materials were produced with medium-rapid cooling rates, estimated by Finite Elements Simulations.
- Microstructural features were evaluated in the view of possible application as Latent Heat Thermal Energy Storage form-stable systems.
- Thermal responses were modeled by thermodynamic calculations and assessed by Thermal Analyses.
- The form stability of the composites was assessed by dilatometric tests.

GRAPHICAL ABSTRACT
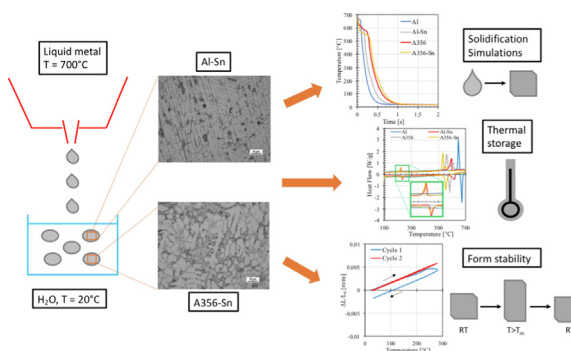
ABSTRACT

The aim of the work was to explore the possibility of producing Sn-bearing composite phase change materials (C-PCMs) intended to be used as Latent Heat Thermal Energy Storage (LH-TES) systems. To this purpose, pure Al and A356 Al alloy, with 40%mass Sn, were produced by granulating process. They were composed by an Al (and other phases) matrix and a low melting Sn-rich phase that can store/release latent heat by its melting/solidification. Pure Al and A356 were produced as reference materials. Finite Element Analyses was used to estimate the cooling rate experienced by the alloys during granulation. Microstructural features of the produced materials were discussed as for C-PCM. Granules thermal characterization was performed with Differential Scanning Calorimetry and dilatometry tests.

Results show that Sn addition delays the solidification and increase microstructural refinement. Phase transition of the Sn-rich phase occurs at about 230 °C in Al-Sn alloy and in the 200–230 °C range for A356-Sn alloy, as also assessed by CALPHAD modelling. The stability of the thermal response for all the systems, as well as the form stability, is achieved after the first cycle. Moreover, A356-Sn exhibits suitable microstructure for limiting the exudation of the Sn-rich phase, making this alloy very attractive for C-PCMs.

1. Introduction

The Al-Sn binary equilibrium phase diagram is characterised by a miscibility gap, which results in two phases at any temperature below solidus line: pure Al and Sn with small amount of Al as solid solution [1,2]. Alloys with this behavior are referred as immiscible

* Corresponding author.
  E-mail addresses: paola.bassani@cnr.it (P. Bassani), matteo1.molteni@polimi.it (M. Molteni), elisabetta.gariboldi@polimi.it (E. Gariboldi).

or Miscibility Gap Alloys (MGAs) [3–5]; the solidified alloy can be considered as a composite material, made of two metallic phases. This feature has been exploited for applications such as bearing materials, in which the dispersed soft Sn phase acts as solid lubricant for the though Al matrix [6,7]. More recently, Sugo et al. [5] suggested the use of Al-Sn immiscible alloys as Phase Change Materials for thermal energy storage. Heat is stored/released during the melting/solidification of Sn; the liquid phase is mostly formed of Sn in a relatively wide temperature range (some tens of K), without significant solution melting of Al matrix, giving microstructural stability to the PCM.

Indeed, a so called "inverse microstructure" [3], similar to that found in bearing alloys in which Sn is dispersed in a continuous Al matrix, is suitable for PCM composites. In particular, it prevents leakage of molten Sn, imparts form stability and residual mechanical properties above Sn melting temperature, and it improves the effective thermal conductivity. However, the content of Sn in bearing alloys is limited (up to about 20% wt.); higher amount of active phase has to be sought for PCM purposes. For high Sn content, proper microstructure was achieved by techniques like powder metallurgy [5,6,8,9] or cold spray [10], in which powders of homogeneous or pre-mixed Al and Sn phases were adopted.

Conventional melting proved to be not suitable to obtain inverse microstructure, due to segregation of Sn at Al dendrites boundaries favored by low cooling rates. On the other hand, casting with inoculants [11], with the application of magnetic field [12–14] or pressure [15] and/or rapid solidification processes (including thermal spray [7,16], melt spinning [17,18] and powder bed laser melting [19,20]) led to microstructural features closer to the targeted microstructure. Unfortunately, the last processes involve very high solidification rates (from 10^3 to 10^7 °C/s [7,12]) and are quite expensive. Possibly, milder solidification rates could be sufficient to achieve the desired inverse microstructure or at least sufficiently thin interdendritic regions, that are less permeable [21–23] to the molten active phases of C-PCMs, thus limiting the potential Sn leakage, which threatens the PCM cyclic storage performances. At the same time, the obtained microstructure has to grant the form stability of the composite under repeated phase transitions [24]. However, no information was found in literature about processes involving intermediate cooling rates.

Thus, in the present work water granulation [25–27] was considered for Al-Sn-based PCMs production. This process has been applied in the historical jewellery [28] and in updated versions is nowadays widely used to produce master alloy granules, also termed shots, for goldsmith market. The molten metal is poured through a small nozzle into a cooling media (generally flowing water) so that it solidifies into granules. Contrarily to atomization processes, no spraying action is applied, and rather coarse particles are produced. Intermediate cooling rates between conventional casting and rapid solidification processes, i.e., powder bed laser melting, are expected.

The authors intended to explore the effectiveness of water granulation to realize suitable Sn-bearing systems for C-PCMs through rather high cooling rates. The eventual suitability of such a technique and the proper analysis of the imposed cooling rates, will also enable the authors to identify other possible technologies for the production of near net shape functional products.

Additionally, no references were found about the evolution of more complex systems, in which Al alloys are considered in place of pure Al, in view of possible industrial exploitation of Al Alloys-Sn systems as C-PCM.

Granulating process was hence applied to the binary Al-40% mass Sn as well as to the system obtained from a commercial Al alloy, specifically the widely used Al-7Si-0.4 Mg casting alloy (A356 alloy). This alloy was considered due to its widespread availability, also in the form of scraps. Additionally, it is an age harden-able alloy, providing potential for the increase of the matrix strength. As Sn source, commercially pure Sn bars were used. Again, an amount of 40% mass content of Sn (corresponding at about 20%vol) was considered also for this system. Pure Al and A356 alloy were granulated too, as reference materials for modeling purposes.

Granules were characterized by means of visual inspection, size, morphology and density measurements, optical microscopy, scanning electron microscopy, calorimetry and dilatometric tests. Finite Elements Analysis was used to estimate the process cooling conditions. The effects of chemical composition and thermochemical properties of the alloys on solidification rate and microstructure, thermal response and form stability were investigated with the aid of CALPHAD modelling and discussed.

2. Materials and methods

2.1. Materials production

Four compositions were considered for water granulation process: Al and A356 alloy, as reference systems, and the corresponding alloys obtained by adding 40% mass Sn (roughly corresponding to 20% vol. for both systems). The starting materials were commercially pure Al ingot, A356 casting alloy parts [29] and extruded commercially pure Sn99.85 alloy (BS EN 610: 1996), supplied as bars with $8X5mm^2$ rectangular section. Their chemical compositions as given in the material supply documents, and the calculated ones for the 40% Sn-containing alloys, hereafter referred as Al-Sn and A356-Sn, are presented in Table 1.

The raw materials were reduced to small pieces, cleaned with acetone, and weighted to a total casting mass of about 150 g. Water granulation process was performed with an Aseg Galloni VCM III induction melting machine. The alloys were molten in a graphite crucible, under protective Ar atmosphere. The same casting temperature of 700 °C was considered for all the systems: once the molten alloy reached this temperature, it was poured in the water granulation unit of the system, through a nozzle of 3.6 mm diameter. Metal stream fell in a water-10 vol% ethanol solution, at room temperature, kept in smooth motion by a recirculation pump.

2.2. Granules and microstructural characterizations

Size and morphology of about 50 granules, whose shape was similar to red blood cells, or broad beans, for each of the four investigated materials, were quantitatively analysed. Three thicknesses values were measured for each granule with a digital calliper. Additionally, aspect ratio, minimum, maximum and equivalent diameter, were also obtained by ImageJ software [30].

Mass and density of granules were measured using an Analytical Balance ME204 and the Density Kit Standard and Advanced (Mettler Toledo), respectively. Measurements were repeated three times. Selected granules were mounted with hot resin and grounded to about half thickness for microstructural investigation. The metallographic polishing was completed by a final step with colloidal silica. Microstructures were observed with optical microscope (Leitz Aristomet Optical Microscope, equipped with polarizing/analyzing filters (Leica), and a DS- Fi3digital camera (Nikon), operated by Elements (Nikon) software). More microstructural details were also obtained by observation with Field Emission Gun Scanning Electron Microscopes (FEG- SEM) (Zeiss Sigma 500 and Hitachi SU70), from Backscattered Electrons (BSE) and/or Secondary Electrons (SE) signals. To gather information on cooling rate effect on microstructure, a quantification of the Sn content was attempted from evaluation of bright areas in BSE images, and Secondary Dendrite Arm Spacing (SDAS) of primary solidified Al-phase

Table 1
Chemical composition (mass%) of investigated alloys (n.c.: not calculated).

	Sn	Al	Si	Fe	Mn	Mg	Zn	Ti	Other, 1	Other, 2
Al	–	99.93	0.030	0.095	0.002	0.003	0.004	0.001	–	–
A356	–	91.91	7.37	0.14	0.007	0.41	0.003	0.12	B 0.037	Sr 0.015
Sn	99.96	–	–	0.0049	–	–	–		Pb 0.011	Sb 0.010
Al-Sn (calc.)	39.84	60.06	0.018	0.057	0.001	0.002	0.02	0.0006	-*	-*
A356-Sn (calc.)	39.87	55.28	4.43	0.082	0.004	0.237	0.002	0.069	-*	-*

* Not considered.

were calculated on 4–5 differently sized granules for each alloy, focusing the analyses in the intermediate region, between the skin and the central zone. For each SDAS measurement, the length of a reference line was divided by the number of intersecting secondary dendrite arms [31].

2.3. Thermal characterization

Thermal characterization of the alloys up to completion of melting were performed with Differential Thermal Analyses tests (Simultaneous Differential Thermal Analyzer SDT Q600, TA instruments) on specimens of 40 mg mass, from RT to 700 °C and back to RT, with a 5 °C/min heating/cooling rates.

Differential Scanning Calorimetry (with DSC25, TA instruments) tests, were performed to evaluate thermal heat storage properties and their stability over cycles involving the melting of the active phase(s) only. Tests were conducted in argon environment on ∼55 mg mass samples in the temperature range RT-300 °C, with heating and cooling rates of 2, 5, 10 and 20 °C/min. Further tests consisting of repeated RT-300 °C-RT cycles at 10 °C/min for Sn bearing alloys were performed on as-produced alloys to test thermal response stability.

The form stability of the materials was checked by means of dilatometric tests (Linseis L75 Vert dilatometer) performed on 4X4X10mm samples machined from granules. Two RT-270 °C-RT cycles with heating/cooling rates of 2 °C/min were carried out in vacuum.

2.4. System modeling

Modeling of the expected phases and solidification rates was also performed. Simplified chemical compositions were considered; Al and Sn for Al-Sn alloy, Al-Si-Mg-Fe-Ti for A356, and Al-Si-Mg-Fe-Ti and Sn for A356-Sn.

For each of the investigated metallic systems, thermophysical properties of interest for PCM composite materials such as latent heat of fusion, specific heat, theoretical density, phases amount (in mass %) at different temperatures and solidification ranges were calculated using CALPHAD-based Thermo-Calc Software [32].

As far as the Sn-containing alloys are concerned, also the amount of Sn included in the α-Al phase and vice-versa were computed at the completion of solidification.

The calculations were performed in both equilibrium solidification and at three cooling rates (0.1–2–300 K/s), using a Scheil solidification model, in order to understand the influence of the cooling rate on the aforementioned parameters.

Detailed results for Al-Sn and A356-Sn systems in all the investigated conditions are reported in Tables A1, A2 and Figs. A1, A2 of Additional Data, respectively.

2.5. Cooling rate modeling

Simplified FE simulations on the solidification of the granules were performed in order to understand the differences in the solidification rates experienced by the pure Al and the three alloys during water granulation process. Comsol Multiphysics software 5.6 was used for this purpose.

Temperature-dependency of density (ρ) and specific heat (C_p), required as inputs, were computed with Thermocalc in the equilibrium condition for all the materials investigated.

Further necessary input was temperature-dependence of thermal conductivity (k_c). Experimental data surveyed in literature for liquid or solid [33–40], resulted in values for Al, A356 and pure Sn.

However, to the author's best efforts, no data is available for Al-Sn/A356-Sn k_c from the fully liquid to fully solid conditions. Similarly, no reliable models were found in the literature for prediction of k_c in the whole temperature range considered. Recently, the adoption of numerical approaches for the evaluation of k_c in composite structures has taken off [41–43]. However, their complex theoretical background, combined with the high temporal effort required, leads to not ready-to-use results. Consequently, a temperature-dependent analytical model based on the thermal conductivity of the component phases and their relative volume fraction, is proposed.

Hence for the reference Al and A356 alloy, literature data from [26,27] were used.

For the composites, k_c was obtained combining the data surveyed for Al [33], A356 [34] and pure Sn (Yamasue et al. [38] for the solid and Sharafat et al. [39] for the liquid), as described in the result section.

3. Results and discussion

3.1. Differential thermal analysis

This test allowed to determine how Sn addition modifies the phase transformations over the whole solidification process in the considered systems.

Mass-normalized heat flow curves from DTA analyses are reported in Fig. 1, where positive heat flow is referred to exothermic events. For better view, events at around 200 °C are enlarged in the inset. Pure Al shows only the transition related to its melting and solidification, as expected. When Sn is added, in agreement with Al-Sn phase diagram, two thermal events can be detected. At high temperature, Sn presence lowers liquidus temperature and widens solidification range of primary Al dendrites, while at about 230 °C a second event related to eutectic solidification of Al-Sn can be observed, in good agreement with literature (229.6 °C, Chenga et al. [44]) and Thermocalc computed data (Fig. A1). When dealing with A356 and A356-Sn alloys, DTA curves become more complex. At high temperatures, the two alloys show a melting/solidification peak characterized by two humps that can be associated to melting behavior of hypoeutectic Al-Si alloys [45] (melting of eutectic interdendritic constituent and, at higher temperature, melting of primary Al-rich dendrites, Fig. A1b). Both events are shifted to lower temperatures in Sn-containing alloy. At low temperature (below 300 °C), for A356 alloy only a low and broad peak can be detected during heating, whilst A356-Sn alloy shows two well defined peaks, at about 200 °C and 230 °C,
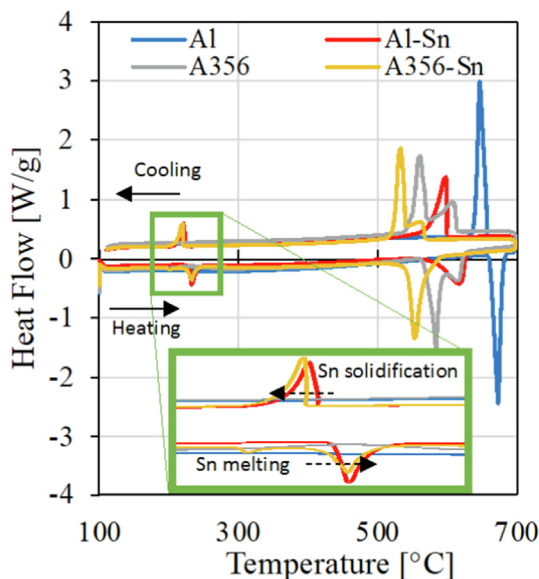
Fig. 1. DTA results: mass-normalized heat flow of the 4 alloys in the temperature range 100–700 °C (heating cooling rate: 5 °C/min).

that can be associated to two different melting/solidification events, coherent with the transition events presented in Fig. A1b. No small and broad peak, similar to that of A356, was observed.

3.2. Granules size distribution and density

The size and shape analyses of the granules are summarized in Table 2: aspect ratio (i.e. maximum to minimum diameter) of 1.2 ± 0.2 was observed for the multicomponent alloys, and slightly bigger (1.4 ± 0.5) for Al. This result allowed to consider the granule shape as an oblate ellipsoid, for further calculations and modelling. For this reason, a unique equivalent diameter d_e, i.e., the diameter of the circle of the same area, was used as size index for the granules, simply referred as 'diameter'. Notably, Al showed much wider size distribution of granules with respect to the other alloys. A356 alloy presented the highest average d_e (11.8 ± 0.2 μm), and the narrowest size distribution, whilst the other alloys have much smaller size.

The experimental average measured density (ρ_{exp}) of the granules, and related standard deviation, is compared to the computed theoretical densities (ρ_{th}) according to thermodynamic calculations in Table 3, together with the porosity percentage, calculated by Eq. (1) [46]:

$$Porosity[\%] = \left(1 - \rho_{exp}/\rho_{th}\right) * 100 \qquad (1)$$

The average porosity is relatively high (more than 4%) in both Al and Al-Sn alloys, while it is lower than 0.7% only for A356 alloy. The tin addition to A356 alloy does not significantly alter the calculated porosity, which remains lower than 2%.

Thus, best results in terms of density and compactness are given by the A356, a material widely employed in the industrial field of

Al-based casting alloys, due to the high fluidity and the compensation of Al shrinkage offered by Si [47]. Indeed, the formation of granules with density values very close to the theoretical ones can be related to the good fluidity of the alloy. The pure aluminium instead, provides rather porous samples. This, in addition to the consistent dimensional scatter, could be related to the fact that the pouring temperature was close to its solidus line. Hence, during the casting, even small reduction of the temperature could have affected more intensively the properties of the melt (viscosity, surface tension) determining strong differences in the size of the granules.

The addition of tin results in a widening of the transition ranges and lowering of the solidification temperature of both Al and A356, as observed by DTA tests and CALPHAD simulations (Tables A1 and A2). This fact results in slightly lower porosity for Al-Sn. The A356-Sn system, present a lower porosity, compared to the latter, as expected due to the better casting properties of A356 compared to pure Al. Even if rather low, porosity of the composite A356-Sn is higher than A356: indeed, the volume reduction of the solidifying Sn-rich liquid may have been hindered by the existing solid, composed of harder Al-rich phase and Al-Si eutectic constituent.

3.3. Microstructural analyses

Representative optical microscope micrographs at low magnification of the three alloys, and scanning electron microscope micrographs at higher magnification of the two Sn-bearing alloys are given in Figs. 2 and 3, respectively. Any dendritic solidification structure could be observed for pure Al, which possibly experienced a dominating planar growth, being a pure metal [48] (Fig. A2). Moreover, no secondary phases or other relevant features are present; for this reason. Thus, Al was not involved in further microstructural analyses.

On the contrary, the corresponding Al-Sn, shown in Figs. 2a and 3a, is characterized by highly elongated primary Al columnar dendrites (SDAS ranging approximately from 3 to 8 μm) sorrounded by interdendritic Sn-rich solid solution (brighter areas in Fig. 3a). This latter is characterized by an extremely fine and hardly noticeble dendritic structure. The microstructure resembles the Al-40 wt% Sn one obtained by K.S. Cruz et al. [49] with directional solidification. Micrometric dark spots can also be observed in Fig. 2a, recognised as voids in SEM micrographs (3a and 3c). Their presence could be traced back to different origins. Some of them, located in the middle of relatively coarse Sn-volumes, are solidification pores formed within the last solidifying regions of the Sn-rich volume due to the exhaustion of molten phase. Others are related to the detachment of isolated Al dendrite arms during polishing (white arrows in the below figures), possibly caused by the poor interaction between the two metals, as stated by their phase diagram [2]. The shrinkage of Sn-rich phase during solidification leaves discontinuities at Al-Al dendrite arms interfaces (red arrows), Al-Sn interface (black arrows) and Sn/Sn dendritic grains (blue arrows). Sub-micrometric pores (green arrows) can further be observed in Sn-rich phase. The presence of the previously listed discontinuities can be related to the pronounced mismatch in the volumetric coefficient of thermal expansion of the two phases in the considered temperature range [39,50,51]. Indeed, this leads

Table 2
Statistical values describing granule size and morphology for each alloy.

	Al	Al- 40% mass Sn	A356	A356- 40% mass Sn
Average equivalent diameter (d_e) [mm]	9.3 ± 0.4	9.1 ± 0.3	11.8 ± 0.2	9.7 ± 0.2
$d_{e,\ min}$	2.9	3.6	9.1	4.0
$d_{e,max}$	13.1	13	14.4	13.9
Thickness Ratio (d_{ei}/t_i)	2.1 ± 0.2	2.4 ± 0.4	2.4 ± 0.2	2.5 ± 0.4

Table 3

Experimental average densities for the investigated alloys compared to their theoretical values according to thermodynamic calculations with Thermocalc [32] and calculated porosity.

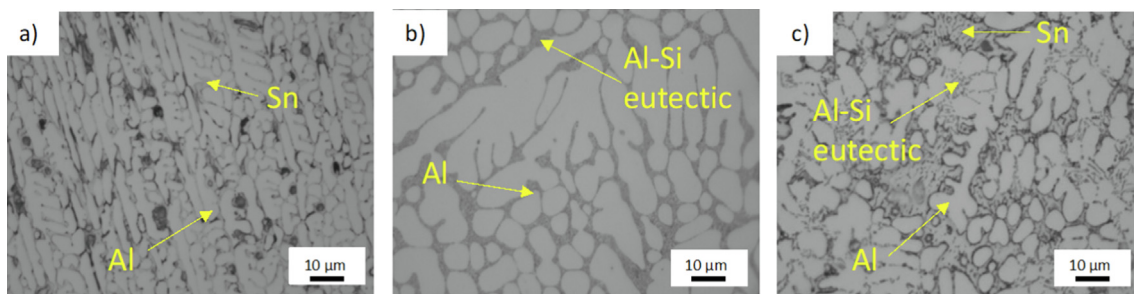| Alloy	Pure Al	Al- 40%mass Sn	A356	A356-40%mass Sn
Experimental average density [g/cm^3]	2.567 ± 0.006	3.454 ± 0.008	2.650 ± 0.002	3.499 ± 0.008
Theoretical density [g/cm^3]	2.699	3.611	2.667	3.560
Average porosity [%]	0.005 ± 0.0002	0.004 ± 0.0002	0.001 ± 0.0001	0.002 ± 0.0002

Fig. 2. Representative low-magnification micrographs (1000x) (light microscope) of the microstructures of: Al-Sn, (a), A356 (b) and A356-Sn (c).
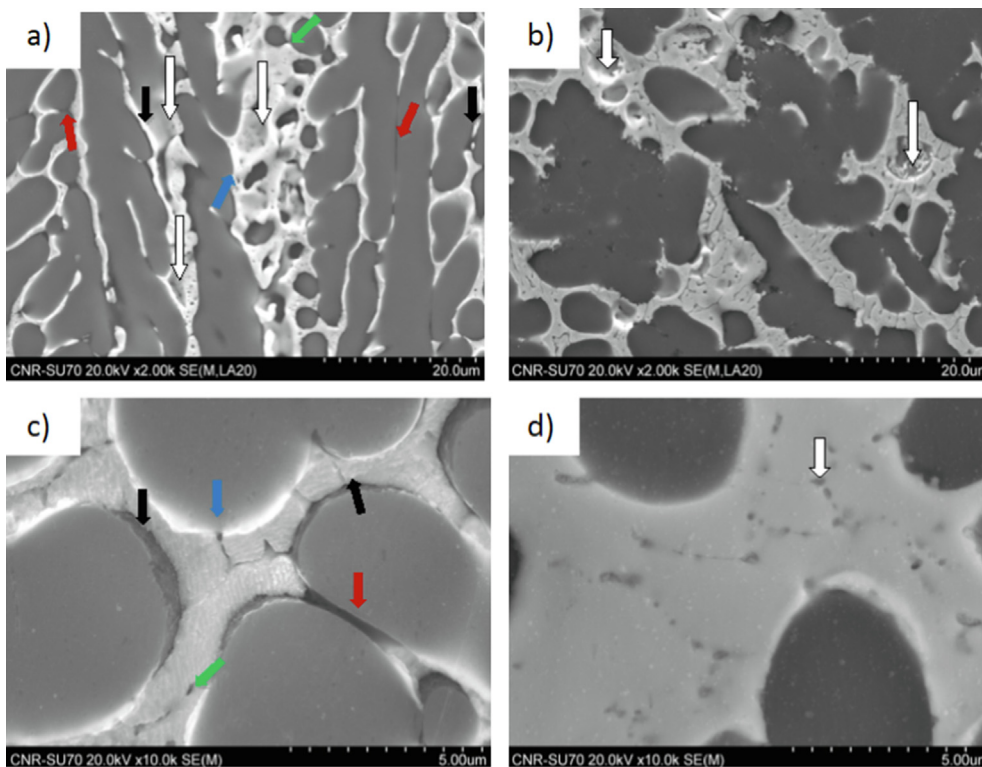

Fig. 3. SEM high-magnification micrographs representative of the microstructures of the Sn-containing alloys: Al-Sn, 2000x (a); A356-Sn, 2000x (b); Al-Sn, 10,000x (c) and A356-Sn, 10,000x (d). Arrows point at details discussed in the text.

to a difference of volumetric shrinkage of 1.2% between Al (lower shrinkage) and Sn in the solidification range of the granule, that reduces to 0.27% in the fully solid state of the composite, explaining the presence of Sn-free interdendritic areas. Moreover, the high solidification shrinkage of the Sn itself, 2.3%, can justify shrinkage voids and discontinuities in this phase.

A356 alloy (Fig. 2b), exhibits more equiaxic α-Al dendrites with respect to Al-Sn, with SDAS in the range 5–11 μm, possibly promoted by the addition of the refiners in the alloy [52]. Al-Si eutectic compound with globular appearance in interdendritic regions [53] can also be observed in the optical micrograph. Its globular configuration is related to the presence of modifiers [54] and favoured also by cooling rates higher than conventional castings.

A356-Sn alloy displays a primary Al-dendritic structure (Fig. 2c) with SDAS in the range 3–8 μm, possibly refined, with respect to A356, due to the action of Sn [55]. In this case, the interdentritic region is characterized by the presence of two mixed structures: Sn-rich solid solution and Al-Si eutectic structure, also not acicular. The two structures alternate in the interdentritic regions, leading to confiment of Sn phase. This situation is very interesting because

it is potentially limiting the exudation of the low melting phase, making this alloy very attractive for C-PCMs. Sn phase is also characterized by a dendritic structure, with the presence of further, nanometric interdentridic phase with lamellar structure, typical of eutectic compounds (Fig. 4a and b).

As far as Sn-rich phase content, a quantification measurement was attempted on BSE images of SEM observations. Sn content demonstrates to be practically independent from the size of the granule. This suggested that the cooling rate, correlated to the size of granules, has no effect on the active phase content, which determines the heat storage capability when C-PCM undergoes transition. The results seem to be in accordance with Thermocalc calculations in non-equilibrium condition (Tables A1 and A2); they do not provide directly the phase content, but they show that the Al content in Sn-rich phase is not affected by cooling rate in the range 0.1–300 °C/s.

The microstructures observed for Al and the three investigated alloys can be directly correlated to the solidification path supplied by thermodynamic calculations and by the differential thermal analyses (Figs. A1 and 1).

The double peaks occurring at higher temperatures in the Si-containing alloys (A356 and A356-Sn) are related to the development of the high-temperature solidification structure, i.e., the dendritic growth of α-Al dendrites followed by the Al-Si eutectic. The presence of small amount of other elements, Ti in particular [52,56], acting as nucleation points, contributed to a finer structure in A356-based alloys. A356-Sn shows an extra peak close to 230 °C in the heating stage with respect to its counterpart without tin, identified as the melting of Sn-rich phase. Moreover, another peak close to 200 °C is visible. This could be related to the melting of a eutectic phase, as those found inside Sn-rich phase (Fig. 4). Its presence was predicted by Thermocalc [32] (Fig. A1b) and can be referred as either Mg_2Sn or Mg_2Si, that share the same crystal structure [57]. The lamellar appearance [58], in addition to the lower Gibbs Free Energy [59] and the element distribution detected by EDS spectra (Fig. A3 in the Additional Data), suggests the eutectic to be identified as Sn-Mg_2Sn.

To conclude, Al-Sn does not seem to be the most promising solution for heat storage purposes, since the well-developed Sn interdendritic channels possibly offers a preferential path for a consistent exudation of the active phase when it melts. Its leakage limits the performances of the C-PCM, reducing the amount of storable heat. Moreover, the defects seen in the micrographs, already present in the as-produced condition, may lead both to form-instabilities and to a reduction of the thermal conductivity of the C-PCMs.

On the other hand, A356-Sn microstructure is more similar than Al-Sn to the desired "inverse" one. Indeed, among the metallic system studied, the Sn-containing casting alloy presented the most homogeneous microstructure with equiaxed primary α-Al dendrites and discontinuous Sn-rich islands interrupted by interdendritic eutectic Al-Si, which is a favorable microstructure for form stable C-PCMs.

The microstructural coarseness, related to the potential mobility of the active phase [21–23], was taken into account. In order to achieve such a purpose, Secondary Dendrite Arm Spacing (SDAS) were evaluated for granules of different dimensions, experiencing different cooling rates.

Values for SDAS, mentioned in the microstructural description, are the average median values of cumulative distribution of SDAS for granules of different sizes, reported in Table 4. As additional output, it was possible to observe that distributions are rather steep, denoting similar cooling condition in the whole specimen. Representative SDAS distribution graphs for the three alloys are provided in Fig. 5, in which the arrows represent the range of median values for each alloy.

3.4. Cooling curves simulation and cooling rate correlations

3.4.1. Thermal conductivity modelling for Sn-bearing alloys

The temperature-dependence of thermal conductivity (k_c) was modelled on the basis of k_c experimental data surveyed in literature for liquid or solid metals and alloys [33–40].

For Al, the temperature description of k_c, given by Brandt et al. [33], was selected. For A356, data by Overfeld et al. [34] were used. However, to the author's best knowledge, no data is available for Al-Sn/A356-Sn k_c from the fully liquid to fully solid conditions. Similarly, no reliable models were found in the literature for prediction of k_c in the whole temperature range considered.

For these reasons, a multi-step model is proposed, considering the three different conditions encountered by the alloys during solidification: fully liquid, solidification, and fully solid ranges. In all the cases, k_c of the composite was obtained combining the literature data surveyed for Al [33], A356 [34] and pure Sn (Yamasue et al. [38] for the solid and Sharafat et al. [39] for the liquid), considering mass fractions when the system is composed of only one phase (liquid), and volume fractions when at least one phase is solid.

The Sn-bearing alloys, in their fully liquid state, were modelled as solutions, consisting in a solvent (1-indexed) and a solute (2-indexed), accordingly to Filippov and Novoselova's empirical formula [60].

$$k_{liq} = k_1(1 - n_2) + k_2(n_2) - 0.72(k_2 - k_1)(1 - n_2) * (1 - n_2) \qquad (2)$$

where k_{liq} is the thermal conductivity of the liquid phase [W/(mK)], k_1 and k_2 are solvent/solute thermal conductivities [W/(mK)], n_2 is the mass fraction of the solute.
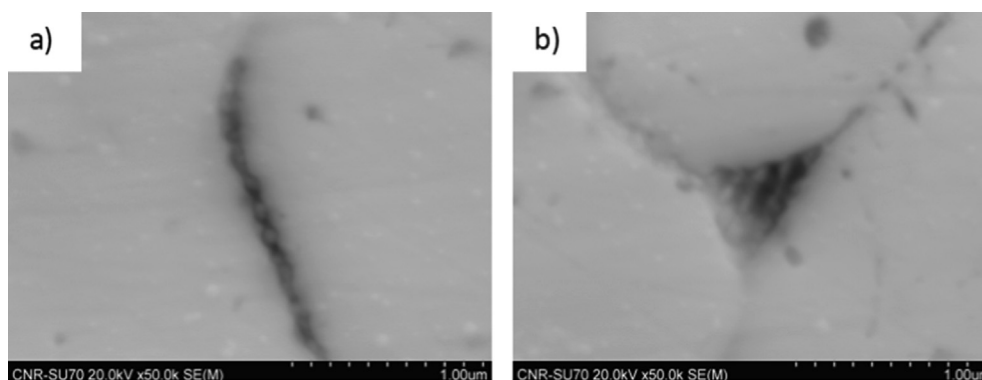

Fig. 4. High-magnification micrographs of the inhomogeneities dispersed in the Sn-rich phase in A356-Sn.

Table 4

Diameter (D) and median SDAS (m-SDAS) value for representative investigated granules.

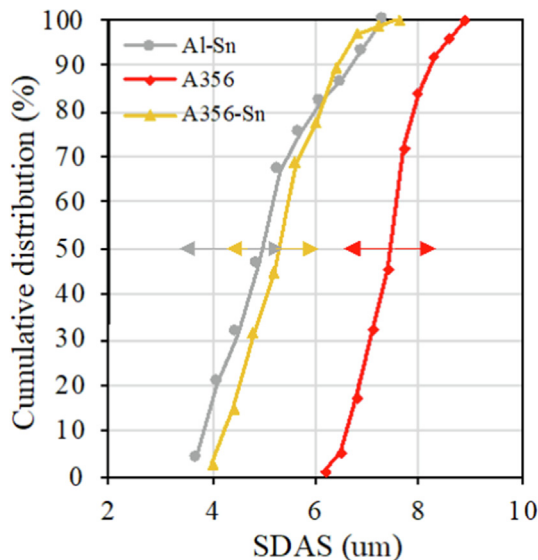| Al-Sn		A356		A356-Sn	
D [mm]	m-SDAS [μm]	D [mm]	m-SDAS [μm]	D [mm]	m-SDAS [μm]
6.33	3.1	9.58	6.8	5.68	4.2
8.33	4.6	11.14	7.3	8.56	4.4
9.10	4.8	12.55	7.4	8.82	5.2
9.15	5	13.04	8.1	9.37	5.6
11.13	5.2			11.11	5.8

Fig. 5. Cumulative distributions of the secondary dendrite arm spacing (SDAS) for granules of Al-Sn, A356 and A356-Sn alloys.

In the fully liquid range, Al/A356 were considered as the solvent and Sn as the solute of the studied system.

In the solidification and solid temperature ranges, two phases coexist: for such systems, thermal conductivity depends also on the phases morphology and relative arrangement [61]. The thermal conductivity was hence modelled on the bases of theoretical upper and lower Wiener bounds for two-phase systems [61]:

$$\text{upper bound } k_{c,u} = k_{Al}V_{Al} + k_{Sn}V_{Sn}$$

$$\text{lower bound } k_{c,l} = \frac{k_{Al}k_{Sn}}{k_{Al}V_{Sn} + k_{Sn}V_{Al}}$$

In the solidification range, k_{Al} and k_{Sn} are referred to pure Al/A356 and Sn-rich liquid thermal conductivities [W/(mK)]. The data of Al/A356 were taken from literature [33,34], whereas the Sn-rich liquid was computed as k_{liq} with the aforementioned Filippov and Novoselova model, considering Sn as the solvent. V_{Al} and V_{Sn} corresponds to the volume fractions of Al/A356 and Sn-rich liquid, computed with Thermocalc in equilibrium conditions. Since the thermal conductivity ratio between the Al/A356 and Sn phases does not exceed 10 in the whole temperature range, the difference between upper and lower bound of thermal conductivity does not exceed about ±15%. Moreover, microstructural analyses revealed a complex microstructure, not easily pointing at one of the two bounds. Under these conditions the morphology dependence of k_c was neglected, and the values of $k_{c,u}$ and $k_{c,l}$ were averaged, and the mean value considered as the effective thermal conductivity of the C-PCMs in the ranges considered.

In the fully solid range instead, k_c was modelled on the bases of solid k_{Al} and k_{Sn}, gathered from literature. V_{Al} and V_{Sn} are the cor-

responding volume fractions, 0.8 and 0.2 in the whole range, respectively. As in the case of the solidification range, k_c for the fully solid state was computed with the aforementioned approach.

The gathered thermal dependency of k_c of pure Al, pure Sn, A356 alloy, and the calculated ones for Al-Sn and A356-Sn are presented in Fig. 6. k_c of the different pure metals/alloys in the liquid state is given as open symbols, whereas crosses were used for the solidification temperature range and solid symbols for the fully solid state (below about 660–550 °C for Al and A356 alloy, below 230–200 °C for the corresponding Sn-containing alloy to be used as C-PCMs).

The addition of Sn to Al and A356 sensibly reduces their thermal conductivity in the solid state, as obvious, but also affects the thermal conductivity in the solidification temperature regions.

3.4.2. Simulation of solidification and cooling

FE simulations have been carried out in order to understand differences in the solidification and the cooling rates experienced by Al and the three alloys during water granulation process. Particles were modelled as oblate ellipsoids, on the bases of the quantitative analysis previously performed (Tables 2 and 4). The temperature at the starting of cooling was considered homogeneous through the granule and equal to 670 °C, thus assuming a limited loss in temperature occurring in molten alloy before reaching the cooling media. A total time span of 2 s was examined. Convection at metal surface was considered as boundary condition, with a constant convection index (h, in W/(m²K)) and environment temperature of 20 °C. For each granule geometry, the simulated cooling profile
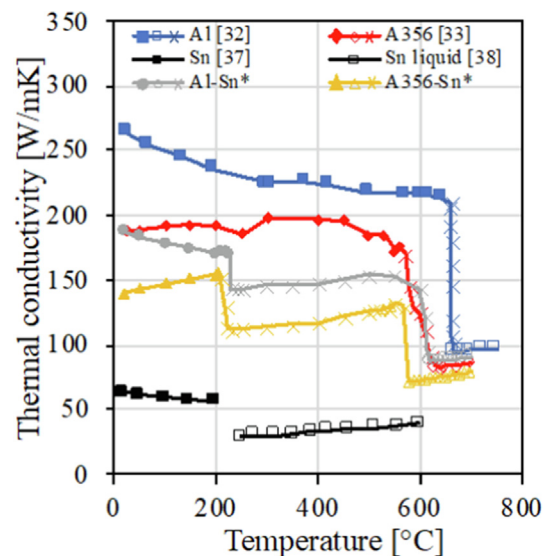
Fig. 6. Temperature-dependence of thermal conductivity for the investigated systems, as well as for pure tin. Literature and calculated with the approach described in 3.4. thermal conductivity values (i.e., Sn-bearing systems, pointed out with *) are presented with solid symbols for fully solid range, open symbols in fully liquid range and crosses in solidification ranges.

was obtained for the point on the rotation axis and at ¼ of thickness from the outer surface. From it, the average cooling rate in the temperature range during which primary aluminum dendrites formed was calculated, considering the corresponding temperature range from experimental DTA tests.

The value of h was identified on the basis of a preliminary set of simulations, performed for A356 alloy. For this alloy a well-established cooling rate-SDAS relationship was available [62,63]:

$$SDAS = 39.4 \cdot R^{-0.317} \qquad (5)$$

where SDAS is the secondary dendrite arm spacing (in μm) and R is the mean cooling rate (°C/s) during solidification of the primary Al dendrite cells. Eq. (5) was used to calculate the (average) cooling rate R for selected granules of different size. Then, simulation of these granules with various h were performed in order to gather calculated R values. A good fitting between experimental SDAS-derived R (horizontal lines in Fig. 7a) and FE calculated ones (points in the same Fig. 7a) was obtained for h values in the range 15,400–

17,300. The value of 16,000 W/m²K was selected for FE simulation of solidification/cooling process for granules of all size/alloys.

Representative cooling curves for Al and the three alloys are presented in Fig. 7b for actual granules with diameters ranging from 8.3 to 9.3 mm. The temperature as function of time drops fast and continuously. The cooling slows down in the transition ranges where the latent heat is released during solidification. The temperature of the transition range detected in simulated cooling profiles are in accordance with the phase changes observed in the DTA curves and CALPHAD-based modeling. More precise results could be obtained further optimizing the models adopted for the changes of thermal conductivity as function of temperature. Anyway, as previously mentioned, to the authors' knowledge, in the literature there's a shortage of mathematical models developed for its evaluation, especially for fully liquid conditions and transition ranges.

Comparing Al and the three alloys, trends are in agreement with the alloy thermal conductivity in the range of Al dendrite solidification temperatures. Indeed, A356-Sn experienced the lowest
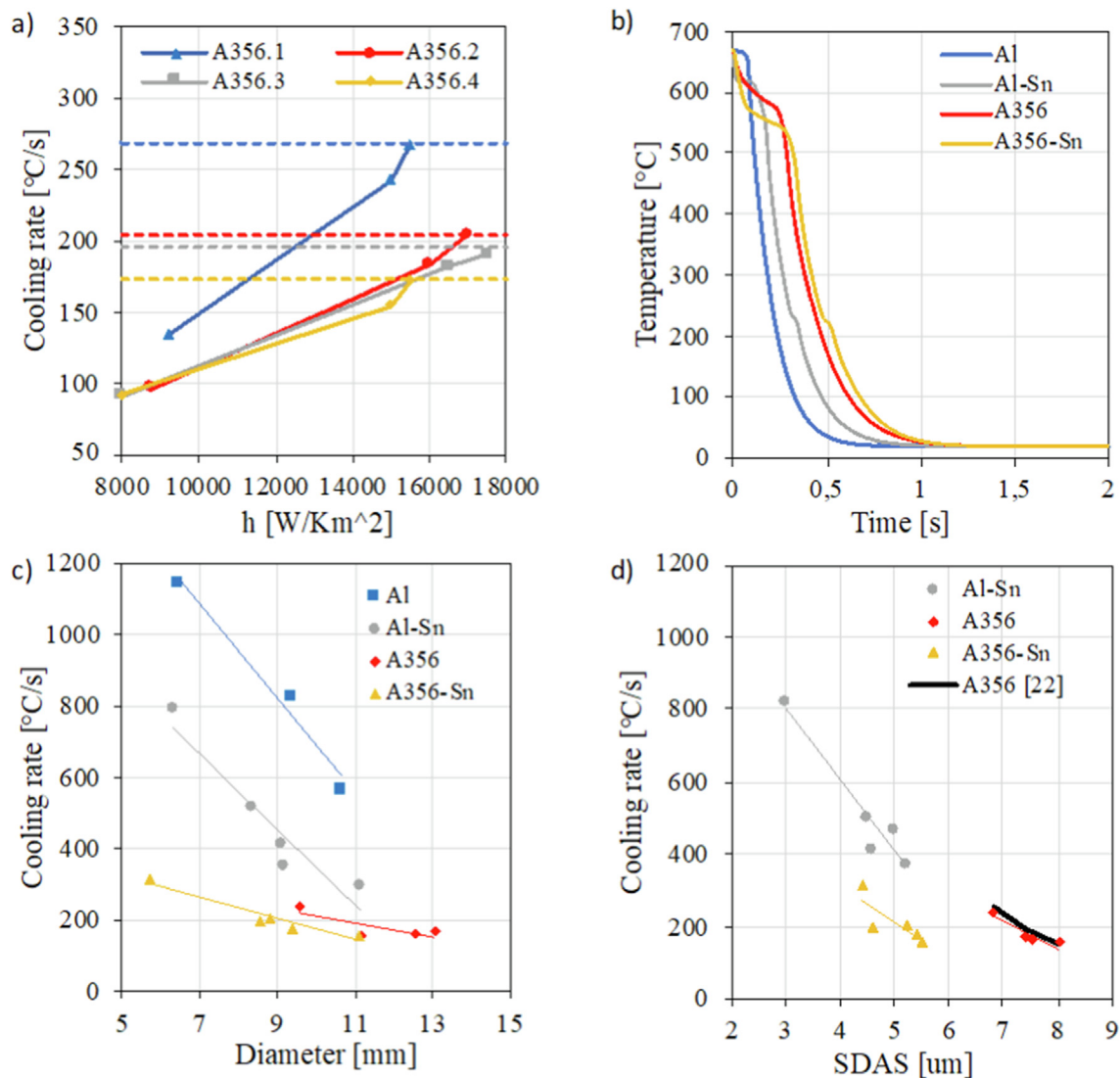

Fig. 7. (a) h-dependent calculated FE-derived cooling rates (points) compared to SDAS-derived cooling rates (horizontal lines) intercepting at h close to 16,000 W/m²K for four considered granule sizes (A356.1 d = 9.58 mm, A356.2 d = 11.14 mm, A356.3 d = 12.55 mm, A356.4 d = 13.04 mm); (b) Representative cooling curves for granules of the investigated Al and metallic systems with similar diameters (Al: 9.29 mm, Al-Sn: 8.33 mm, A356: 9.58 mm, A356-Sn 8.56 mm); (c) Dependence of the cooling rate on the granule diameter during primary Al solidification for the four systems; (d) Correlation between Al-dendrite SDAS and cooling rates for the three investigated alloys. The black solid line for A356 alloy represents the literature correlation adopted to calibrate h values [62].

solidification rate, followed by A356, Al-Sn and pure Al, at fixed SDAS/diameter.

The data in Fig. 7c and d suggest the existence of similar relationships for all the studied alloys between the cooling rate and the SDAS/diameter, in the examined cooling rate range, once proper calibration parameters are chosen. For the granules examined, linear relationships for both diameter-cooling rate and SDAS-cooling rate were found out (Table 5). A detailed study of this relationship was out of the scope of the present paper, and it would have required more defined and controlled cooling environments. With all the limitation of extending interpolating equations to experimental range not overlapping with original ones, the obtained values, for Al-Sn system, of SDAS and cooling rates could fit with results reported in [55]. The results of the h-identification and of FE simulations seem therefore reasonable: the medium–high cooling rates, in the order of some hundreds of °C/s, produce very fine dendritic spacing, i.e., some micrometers. As discussed in Section 3.3, SDAS is indeed influenced by the cooling rate experienced in the process, differently from the content of Sn-rich phase, which remains practically constant. The high evaluated convective coefficient of heat exchange is related to the motion imposed by the recirculation pump to the water bath.

Interestingly, when comparing A356 and the corresponding composites, despite lower SDAS values, the latter present similar simulated cooling rates. It denotes the strong influence of Sn on the refining of the microstructure of the base materials. The results show that cooling rates similar to those experienced in [29], i.e., obtained from the well-known die-cast industrial process, can provide sufficiently high R values to obtain the desired microstructure in C-PCM based on A356-Sn system.

3.5. Differential Scanning Calorimetry and thermal storage potential

The thermal responses of the granules across the low temperature transition were evaluated by means of DSC tests up to 300 °C at different heating/cooling rate and under repeated cycles. The endothermic/exothermic peaks, already noticed in DTA tests, were better observed. Thus, a more precise characterization of thermal properties, especially for Sn-bearing alloys, in view of their use as C-PCMs, is allowed.

The DSC curves at different heating rates are compared in Fig. 8a, b and c. Pure Al was not involved in these tests, since no transition or thermal events in the temperature range studied were expected.

In addition to the Sn transition at approximately 230 °C, Al-Sn presents an exothermic hump at first heating cycle (Fig. 8a), whose position drifts to higher temperature at increasing heating rates, as typically observed for precipitation related peaks. Possibly, this latter event is related to the amount of Sn entrapped in Al phase during the solidification, higher than the equilibrium value as stated by Table A1. As expected, the peak disappears further cycling the granule (Fig. 8d). Further, Al-Sn and, to a less extent, A356-Sn, present a series of spikes in the solidification stage and at temperatures below it, caused by instabilities arisen due to the different shrinkage of Al and Sn, seen in the micrographs (Fig. 3). Moreover, as the number of cycles increase, minor multiple broad peaks appear in the cooling curves (Fig. 8d). These are compatible with

Table 6
Storable and releasable heat of the studied metallic systems, in their service temperature interval.

Alloy	Transition	DSC [J/g]	Thermocalc [J/g]
A356	Precipitation peak	19.24	*
Al-Sn	Melting Sn	31.8	24.5
	Solidification Sn	29.03	24.04
A356-Sn	Melting lamellar eutectic*	1.031	14.34
	Melting Sn	22.72	21
	Total of Melting events	***23.75***	***25.34***
	Solidification lamellar eutectic	0.85	13.79
	Solidification Sn	30.84	16.64
	Total of Solidification events	***31.69***	***30.43***

different growth directions of solidifying Sn crystals with respect to α-Al completely surrounding them [64], as well as to a coarsening of small Sn-phase particles [8,19,65]. In this sense, further investigation on the heat-treated microstructures will be performed in the future.

A broad exothermic peak is present in A356 DSC curve during the first heating, absent during the second cycle (Fig. 8b and e). This can be ascribed to precipitation processes in age-hardenable Al alloys initially in non-equilibrium condition [66,67]. No further cycles were performed on A356.

Differently to the DTA curves, the as-produced A356-Sn presents more than two peaks in the range 200–230 °C (Fig. 8c), possibly associated to different extent of spreading of diffusion phenomena, combined with relatively high inhomogeneity of the sample at the DSC specimen scale [68]. However, it is worth mentioning that repeated cycles suppress the splitting of the peaks observed in Fig. 8c, reasonably resulting from homogenization of phases (Fig. 8f). Further cycles, up to 10 repetition, do not affect the onset of the active phase melting in both the Sn-bearing alloys, demonstrating stable thermal responses (Fig. 8d and f).

The values of the stored/released heat in the transformations detected in DSC tests performed with a testing rate of 2 °C/min are rather comparable to those computed with Thermocalc in equilibrium conditions (Table 6). These values, for Sn-bearing alloys also correspond to storable/releasable heat for use as C-PCMs. The mismatch between the experimental and calculated values can be ascribed to the thermal inertia related to the samples and to the non-equilibrium microstructure of these latter.

The proposed Sn-bearing systems are comparable in terms of mass-normalized latent heat to those of low-melting Bi/In/Pb/Sn-based alloys (20–71 J/g), but they provide a solution in a higher activation temperature range (215–230 °C vs 47–199 °C) [69]. To the author's best knowledge, no other systems can be found in this temperature range, apart from Al/Cu/Mg/Zn-Sn alloys obtained only on the bases of Thermocalc calculations without any information on thermal nor form stability [70].

3.6. Dilatometry and form stability

The variation in the length of the specimens with respect to their initial size, measured during two repeated cycles, is presented below as a function of the temperature in Fig. 9 (blue and red curves, respectively). As for DSC characterization, dilatometry tests were not performed on Al. Differences between 1st and 2nd cycle are mainly related to the heating part of the 1st cycle, where precipitation in A356 alloy occurs, (Fig. 9b), and Sn expands during melting, i.e., 230 °C in Al-Sn sample and in 200–230 °C range in A356-Sn sample (Fig. 9a and c, respectively). A progressive deviation from linear trend in all alloys in the high-temperature range can be associated to creep due to contact-assuring compression load, which and accumulates both in the last part of heating, during hold time, and in the first part of cooling. In all specimens the
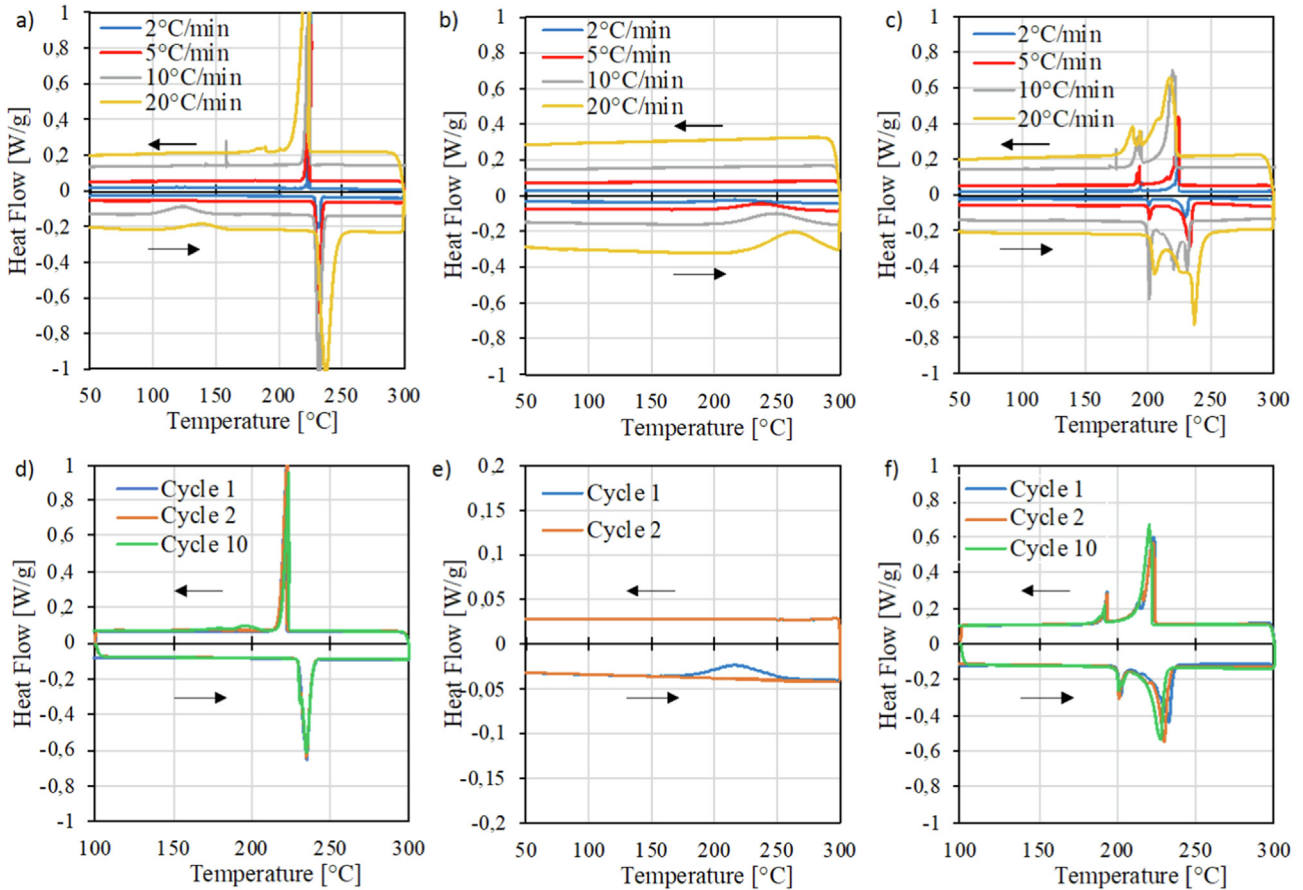
Table 5
Cooling rate dependence on the diameter and on the SDAS of the granules.

Material	Diameter, d-R dependence	SDAS-R dependence
Al	R = -134.12*d + 2031.1	–
Al-Sn	R = -107.14*d + 1418.7	R = −223.63*SDAS + 1472.4
A356	R = -19.8*d + 411.6	[36]
A356-Sn	R = -29.8*d + 471.4	R = −99.6*SDAS + 711.9

Fig. 8. DSC curves representing the mass normalized heat flow as function of the temperature at different heating/cooling rates om as produced Al-Sn (a), A356 (b) and A356-Sn (c). Cyclic DSC tests for Al-Sn (d) at 10 °C/min, A356 (e) at 2 °C/min and A356-Sn (f) at 10 °C/min.
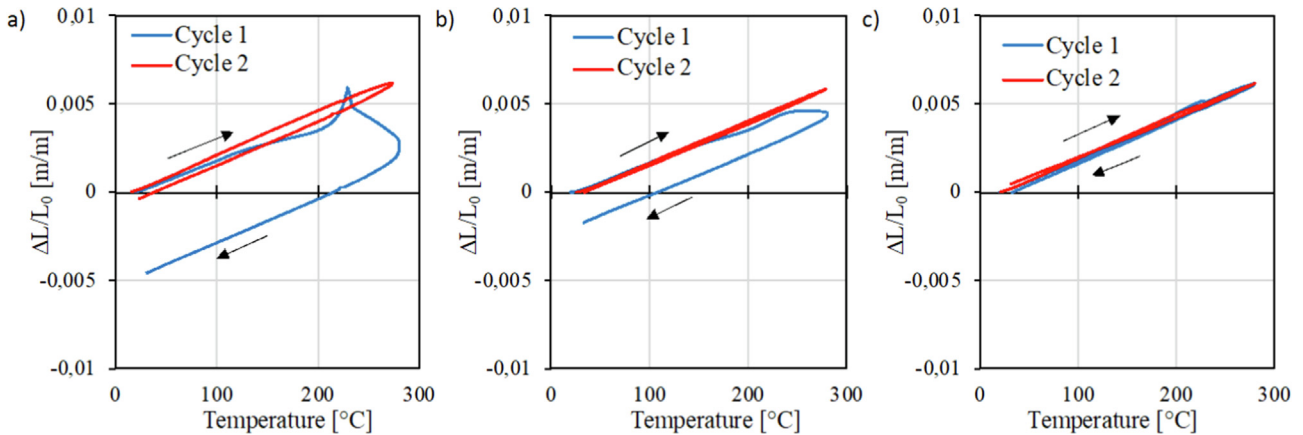

Fig. 9. Sample length variation respect to the initial length ($\Delta L/L_0$) as function of the temperatures in dilatometric tests carried out on Al-Sn (a), A356 (b) and A356-Sn (c) granules. Blue and Red curves refer to the 1st and 2nd cycle on the same specimen tested in vacuum. (For interpretation of the references to colour in this figure legend, the reader is referred to the web version of this article.)

overall creep deformation could have also been affected by minor geometrical imperfections of the sample (such as surface planarity) and, in Sn-bearing alloys, by the reduced mechanical resistance due to the presence of the molten active phase.

The coarse and aligned dendrites in Al-Sn alloy possibly were more prone to relative sliding in presence of molten Sn. Additionally, permanent deformation could also be induced by leakage of active phase. The presence of small droplets of Sn on sample surface already noticed after the 1st cycle agrees with the results of

in-situ microCT analyses for differently processed Al-Sn alloy, in which leakage potential increases with the extension of Sn volumes directly connected to their surface [71].

Among others, A356-Sn alloy is the less affected by the above phenomena during the first thermal cycle. On the other hand, the variation of the length at the end of the second cycle is close to 0 for all the alloys (Fig. 9). Thus, it can be stated that after the stabilization of microstructure, geometry and properties during the first cycle, the Sn-containing C-PCMs alloys are a promising solution in
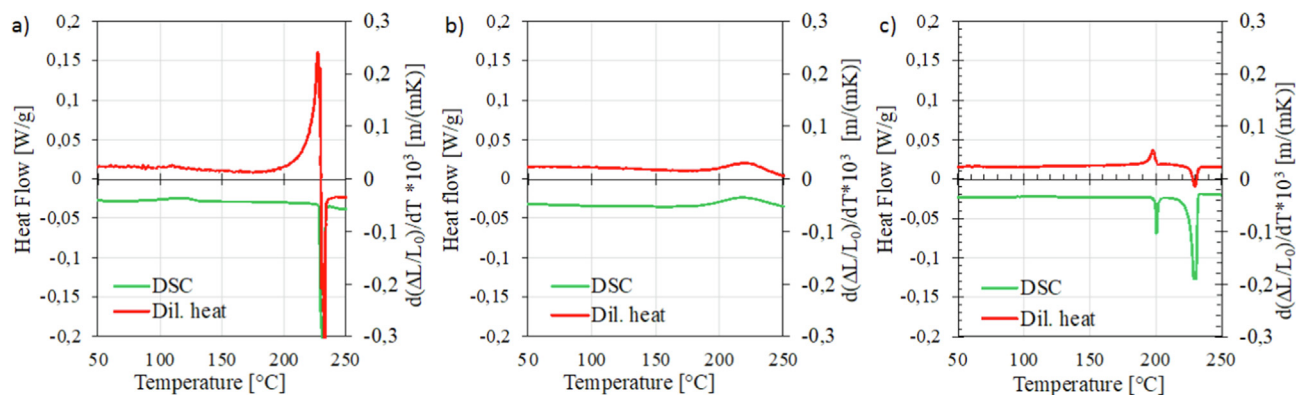
Fig. 10. Comparison between DSC and dilatometer curves – expressed in terms of (ΔL/L₀) first time derivative - for Al-Sn (a), A356 (b) and A356-Sn (c).

terms of form-stability. The melting and solidification of the active phase, still noticeable on dilatometric curves (possibly resulting from modified temperature trends due to the endothermic/ exothermic transformation) do not affect the of thermal expansion, which is not far from that of Sn-free alloys and ais an important feature for the use of these C-PCM materials. In general, additional cycles are reasonably not expected to further modify the length of the granulated Sn-bearing alloys.

The correspondence among the microstructural changes detected in both DSC and dilatometry is highlighted in Fig. 10. The DSC heating curves at 2 °C/min are compared with dilatometric data (heating curves, first cycle) in terms of the first derivative of the length variation/initial length ratio ($\Delta L/L_0$), i.e. instant coefficient of thermal expansion. The curves from the two experiment types present an excellent agreement in the detection of the phase transitions, represented in both cases by peaks deviating from the horizontal linear trend. Their comparison highlights how the sensitivity of the two techniques is different according to the type of transformation and provide complementary information for a comprehensive characterization of phase transition in PCMs.

4. Conclusions

The present study dealt with microstructural and thermal characterization of Sn-containing Al-based alloys (Al-Sn and A356-Sn) produced with water granulation. The main scopes were to understand the potential of these alloys as form-stable composite PCMs and provide experimental results of previously un-explored cooling rate range. The goal was achieved through the combination of experimental characterization campaigns and numerical simulations, based on metallurgical and heat transfer competencies. The reference systems without Sn. i.e., pure Al and A356 alloy, were produced and characterized by the same techniques to evaluate how the addition of Sn affected the material properties, and consequently the processing options. The conclusions can be summarized as follows:

- FE-simulation combined with tests on the reference A356 alloy, allowed to estimate the cooling rate experienced by the materials; highest values of about 800 °C/s were obtained for the smaller granules of Al-Sn, whereas values in the range 150–300 °C/s, close to die-casting process [29], were found for A356 and A356-Sn.
- In the view of solidification simulations, due to the lack of data in literature temperature-dependent thermophysical properties of the Sn-bearing alloys were computed.
- A356 offered the narrowest dimensional distribution and the densest specimens among the four systems. The presence of low-melting phases promoted by Sn addition led to a more scattered geometrical features and slightly higher the porosity.

- The microstructural features of A356-Sn seem to be adequate for heat storage purposes, whilst Al-Sn microstructure favored Sn leakage.
- The DSC tests highlight a potential heat storage of approximately 20–30 J/g, with melting and solidification ranges across about 230 °C for Al-Sn and 200–230 °C for A356-Sn. The stability of their thermal response was demonstrated with repeated cycles.
- Dilatometric tests on Sn-bearing alloys show potential form-stability after the first cycle, particularly promising for A356-Sn.

Data availability

The data that has been used is confidential.

Declaration of Competing Interest

The authors declare that they have no known competing financial interests or personal relationships that could have appeared to influence the work reported in this paper.

Authors contributions

Paola Bassani: Conceptualization, Investigation (Microstructural characterization, DSC, DTA), Resources (Material production), Writing – original draft, review and editing.

Matteo Molteni: Formal analysis (thermodynamic calculations) Investigation (morphological and microstructural characterization, dilatometric tests), Visualization, Writing – original draft, review and editing.

Elisabetta Gariboldi: Conceptualization, Methodology, Validation, Writing – original draft, review & editing.

Data availability

The raw data required to reproduce these findings cannot be shared at this time as the data also forms part of an ongoing study. The processed data required to reproduce these findings cannot be shared at this time as the data also forms part of an ongoing study.

Appendix

See Tables A1, A2 and Figs. A1–A3.

Table A1
Thermophysical properties of interest for Al-Sn alloys obtained from ThermoCalc simulations.

Considered phases	Pure Al (FCC L12) - Pure Sn (BCT _A5)							
Examined condition	Al in Sn phase (% mass%)	Sn in Al phase	Effective density (g/cm^3)	EffectiveSpecific vol. (cm^3/g)	Melting enthalpy (J/g)	Cp (J/ g*K)	Energy released during solidific. (J/g)	Solidificaton range (°C)
Equilibrium 20 °C Completion of solidification after:	0.00041	0.00174	3.611	0.277		0.629	230.41	615.5–590
equilibrium cooling	0.058	0.222	3.559	0.281		0.722	614.8	615.5–229.5
0.1 °C/s cooling	0.231	0.600	3.563	0.281	317.6	0.615		615.6–229.4
2 °C/s cooling	0.232	0.601	3.563	0.281	314	0.615		615.6–229.4
300 °C/s cooling	0.232	0.601	3.563	0.281	314	0.615		615.6–229.4

Table A2
Thermophysical properties of interest forA356-Sn alloys obtained from ThermoCalc simulations.

| Considered Phases	Al matrix (FCC_L12)Sn phase (BCT_A5)Si phase (DIAMOND_A4)AlFeSi phase (AL9FE2SI2)Mg2Sn phase (MG2SI_C1) Al$_3$Sn phase (AL3TI_LT) Al$_3$Ti phase (ALSI3TI2)							
Examined condition	Al in Sn phase (% mass%)	Sn in Al phase	Effective density (g/cm^3)	EffectiveSpecific vol. (cm^3/g)	Melting enthalpy (J/g)	Cp (J/ g*K)	Energy released during solidific. (J/g)	Solidificaton range (°C)
Equilibrium 20 °C Completion of solidification after:	0.00174	0.00041	3.576	0.279		0.621	283.95	570.5–541.8
equilibrium cooling	0.155	0.041	3.533	0.283		0.697	669.53	570.5–203.2
0.1 °C/s cooling	0.165	0.044	3.384	0.296	330.30	0.603		570.5–202.7
2 °C/s cooling	0.165	0.044	3.384	0.296	331.87	0.603		570.5–202.7
300 °C/s cooling	0.165	0.044	3.382	0.262	331.92	0.603		570.6–202.7
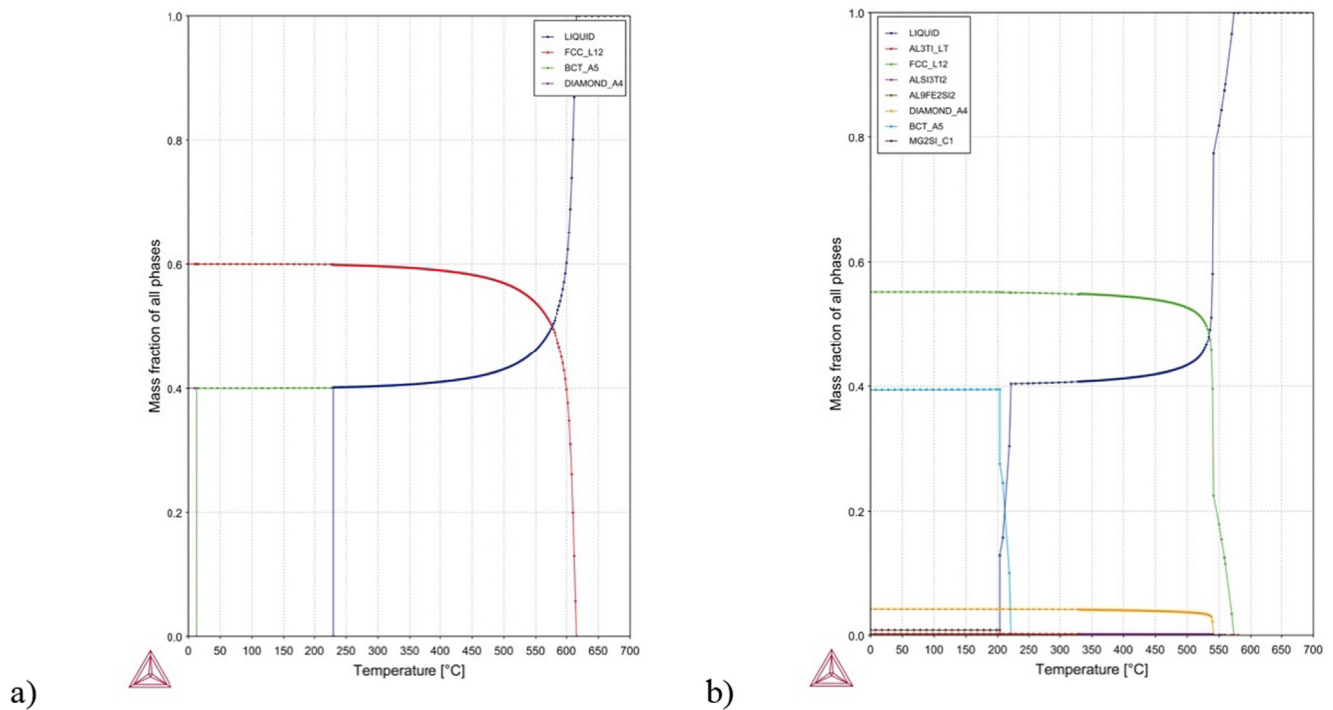
Fig. A1. Temperature vs. phases content predicted by ThermoCalc for Al-Sn (a) and A356-Sn (b) (simplified compositions, equilibrium condition).
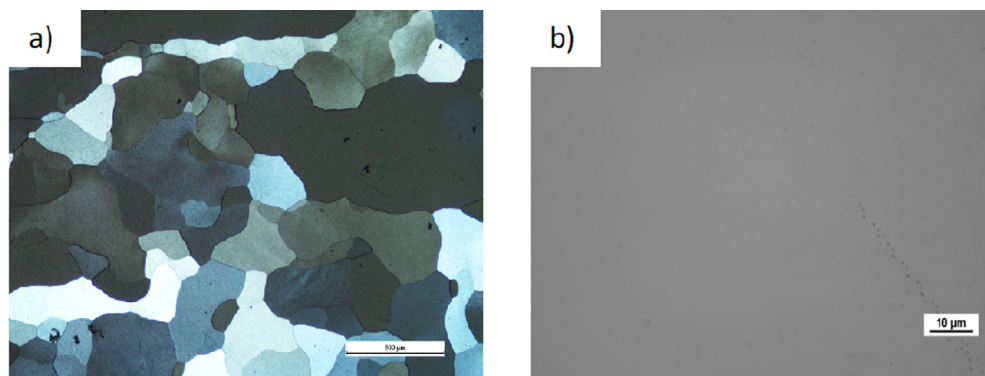

Fig. A2. Optical microscope micrographs for pure Al at different magnifications: (a) 50x with polarized light and (b) 1000x.

References

[1] R. Schmid-Fetzer, Thermodynamic aspects of tin segregation during solidification of aluminium alloys, Mater. Sci. Forum. 618 (619) (2009) 183–190, https://doi.org/10.4028/www.scientific.net/MSF.618-619.183.

[2] A.J. McAlister, D.J. Kahan, The Al-Sn (Aluminum-Tin) system, Bull. Alloy Phase Diagrams. 4 (1983) 410–414.

[3] J. Jie, Z. Zheng, S. Liu, S. Yue, T. Li, Solidification structure evolution of immiscible Al–Bi–Sn alloys at different cooling rates, J. Mater. Res. 34 (2019) 2563–2571, https://doi.org/10.1557/jmr.2019.202.

[4] J.Z. Zhao, T. Ahmed, H.X. Jiang, J. He, Q. Sun, Solidification of immiscible alloys: a review, Acta Metall. Sin (English Lett.) 30 (2017) 1–28, https://doi.org/10.1007/s40195-016-0523-x.

[5] H. Sugo, E. Kisi, D. Cuskelly, Miscibility gap alloys with inverse microstructures and high thermal conductivity for high energy density thermal storage applications, Appl. Therm. Eng. 51 (2013) 1345–1350, https://doi.org/10.1016/J.APPLTHERMALENG.2012.11.029.

[6] X. Liu, M.Q. Zeng, Y. Ma, M. Zhu, Promoting the high load-carrying capability of Al–20wt%Sn bearing alloys through creating nanocomposite structure by mechanical alloying, Wear. 294–295 (2012) 387–394, https://doi.org/10.1016/j.wear.2012.07.021.

[7] T. Marrocco, L.C. Driver, S.J. Harris, D.G. McCartney, Microstructure and properties of thermally sprayed Al-Sn-based alloys for plain bearing applications, J. Therm. Spray Technol. 15 (2006) 634–639, https://doi.org/10.1361/105996306X147009.

[8] C. Confalonieri, M. Perrin, E. Gariboldi, Combined powder metallurgy routes to improve thermal and mechanical response of Al–Sn composite phase change materials, Trans. Nonferrous Met. Soc. China. 30 (2020) 3226–3239.

[9] N.M. Rusin, A.L. Skorentsev, Tribological properties of sintered Al–Sn alloy doped with iron, J. Frict. Wear. 43 (2022) 153–159, https://doi.org/10.3103/S1068366622030126.

[10] X.-J. Ning, J.-H. Kim, H.-J. Kim, C. Lee, Characteristics and heat treatment of cold-sprayed Al–Sn binary alloy coatings, Appl. Surf. Sci. 255 (2009) 3933–3939.

[11] T. Stuczyñski, Metallurgical problems associated with the production of aluminium-tin alloys, Mater. Des. 18 (1997) 369–372.

[12] T. Tamura, M. Li, K. Takahashi, E. Inoue, Improved solidification structures and mechanical properties of Al–20 wt% Sn alloys processed by an electromagnetic vibration technique, Mater. Sci. Eng. A. 862 (2023), https://doi.org/10.1016/j.msea.2022.144416 144416.

[13] S. Li, Y. Li, H. Guo, Z. Wen, Z. Zhu, Effect of electromagnetic stirring frequency on tribological performance and corrosion resistance of Al-Sn bearing alloy, Mater. Today Commun. 32 (2022), https://doi.org/10.1016/j.mtcomm.2022.103898 103898.

[14] S. Li, H. Guo, Y. Li, Z. Wen, Z. Zhu, Effect of electromagnetic stirring current on microstructure and corrosion resistance of Al-Sn Alloy, Mater. Res. Express. 9 (2022), https://doi.org/10.1088/2053-1591/ac6732.

[15] M. Xu, Y. guo Yin, C. min Li, C. chong Duan, A comparative study on Sn macrosegregation behavior of ternary Al-Sn-Cu alloys prepared by gravity casting and squeeze casting, China Found. 20 (2023) 63–70. <https://doi.org/10.1007/s41230-023-2046-1>.

[16] M.E. Makhatha, O.S. Fatoba, E.T. Akinlabi, Effects of rapid solidification on the microstructure and surface analyses of laser-deposited Al-Sn coatings on AISI 1015 steel, Int. J. Adv. Manuf. Technol. 94 (2018) 773–787, https://doi.org/10.1007/s00170-017-0876-y.

[17] M.C. Lucchetta, F. Saporiti, F. Audebert, Improvement of surface properties of an Al–Sn–Cu plain bearing alloy produced by rapid solidification, J. Alloys Compd. 805 (2019) 709–717, https://doi.org/10.1016/j.jallcom.2019.07.082.

[18] W.T. Kim, B. Cantor, Solidification of tin droplets embedded in an aluminium matrix, J. Mater. Sci. 26 (1991) 2868–2878, https://doi.org/10.1007/BF01124815.

[19] C. Confalonieri, E. Gariboldi, Al-Sn miscibility gap alloy produced by power bed laser melting for application as phase change material, J. Alloys Compd. 881 (2021), https://doi.org/10.1016/j.jallcom.2021.160596 160596.

[20] C. Confalonieri, R. Casati, E. Gariboldi, Effect of process parameters on laser powder bed fusion of Al-Sn miscibility gap alloy, Quant. Beam Sci. 6 (2022), https://doi.org/10.3390/qubs6020017.

[21] I. Ngo, C. Byon, Permeability of microporous wicks with geometric inverse to sintered particles, Int. J. Heat Mass Transf. 92 (2016) 298–302, https://doi.org/10.1016/j.ijheatmasstransfer.2015.08.040.

[22] Z. Li, E. Gariboldi, Modelling the conditions for natural convection onset in open-cell porous Al/paraffin composite phase change materials: effects of temperature, paraffin type and metallic structure geometry, Int. J. Heat Mass Transf. 173 (2021), https://doi.org/10.1016/j.ijheatmasstransfer.2021.121279 121279.

[23] J. Feng, J. Fu, X. Yao, Y. He, Triply periodic minimal surface (TPMS) porous structures: From multi-scale design, precise additive manufacturing to multidisciplinary applications, Int. J. Extrem. Manuf. 4 (2022), https://doi.org/10.1088/2631-7990/ac5be6.

[24] Y. Zhang, Z. Jia, A. Moqeet Hai, S. Zhang, B. Tang, Shape-stabilization micromechanisms of form-stable phase change materials-a review, Compos. Part A Appl. Sci. Manuf. 160 (2022), https://doi.org/10.1016/j.compositesa.2022.107047 107047.

[25] K. Forwald, D.C. Rees, Method for granulating molten metal (EP 0 522 844 B1), 1993. <https://www.researchgate.net/publication/269107473_What_is_governance/link/548173090cf22525dcb61443/download%0Ahttp://www.econ.upf.edu/~reynal/Civil wars_12December2010.pdf%0Ahttps://think-asia.org/handle/11540/8282%0Ahttps://www.jstor.org/stable/41857625>.

[26] U. Holding, P.-A. Lundstrom, L.E. Johansson, Apparatus and method for granulation of molten material (EP 3 041 629 B1), 2016.

[27] R. Sridhar, W.L. Shellshear, C.A. Landolt, W. Kantymir, H.L. Schooley, Nickel and cobalt irregularly shaped granulates (US patent 41 68967), 1979.

[28] P. Tan, J. Yang, J. Ji, F. Jiang, Production techniques and microstructures of copper granule: experimental analysis and archaeological case study, Archaeometry. 63 (2021) 826–842, https://doi.org/10.1111/arcm.12649.

[29] L. Ceschini, A. Morri, A. Morri, Effects of the delay between quenching and aging on hardness and tensile properties of A356 aluminum alloy, J. Mater. Eng. Perform. 22 (2013) 200–205, https://doi.org/10.1007/s11665-012-0208-1.

[30] W.S. Rasband, ImageJ, 2018.

[31] M. Warmuzek, Metallographic techniques for aluminum and its alloys, in: G.F. Vander Voort (Ed.), Metallogr. Microstruct., ASM International, 2004, pp. 711–751. <https://doi.org/10.31399/asm.hb.v09.a0003769>.

[32] ThermoCalc, TCS Al-based Alloy Database (TCAL8), 2021, pp. 1–61.

[33] R. Brandt, G. Neuer, Electrical resistivity and thermal conductivity of pure aluminum and aluminum alloys up to and above the melting temperature, Int. J. Thermophys. 28 (2007) 1429–1446, https://doi.org/10.1007/s10765-006-0144-0.

[34] R.A. Overfelt, S.I. Bakhtiyarov, R.E. Taylor, Thermophysical properties of A201, A319, and A356 aluminium casting alloys, High Temp. - High Press. 34 (2002) 401–409, https://doi.org/10.1068/htjr052.

[35] S.I. Bakhtiyarov, R.A. Overfelt, S.G. Teodorescu, Electrical and thermal conductivity of A319 and A356 aluminum alloys, J. Mater. Sci. 36 (2001) 4643–4648, https://doi.org/10.1023/A:1017946130966.

[36] Z. Wang, H. Wang, M. Yang, W. Sun, G. Yin, Q. Zhang, Z. Ren, Thermal reliability of Al-Si eutectic alloy for thermal energy storage, Mater. Res. Bull. 95 (2017) 300–306, https://doi.org/10.1016/j.materresbull.2017.07.040.

[37] B. Giordanego, N. Benazzi, J. Vinckel, J.G. Gasser, L. Roubi, Thermal conductivity of liquid metals and alloys, J. Non. Cryst. Solids. 250 (1999) 377–383, https://doi.org/10.1007/BF02642559.

[38] E. Yamasue, M. Susa, H. Fukuyama, K. Nagata, Deviation from Wiedemann-Franz law for the thermal conductivity of liquid tin and lead at elevated temperature, Int. J. Thermophys. 24 (2003) 713–730, https://doi.org/10.1023/A:1024088232730.

[39] S. Sharafat, N. Ghoniem, Summary of Thermo-Physical Properties of Sn , Comparison of Properties of Sn , Sn-Li , Li , and Pb-Li, (n.d.) 1–51.

[40] F. Meydaneri, B. Saatçi, M. Özdemir, Thermal conductivities of solid and liquid phases for pure Al, pure Sn and their binary alloys, Fluid Phase Equilib. 298 (2010) 97–105, https://doi.org/10.1016/j.fluid.2010.07.015.

[41] C. Liu, R. Qian, Z. Liu, G. Liu, Y. Zhang, Multi-scale modelling of thermal conductivity of phase change material/recycled cement paste incorporated cement-based composite material, Mater. Des. 191 (2020), https://doi.org/10.1016/j.matdes.2020.108646 108646.

[42] H. Kallel, K. Joulain, Design and thermal conductivity of 3D artificial cross-linked random fiber networks, Mater. Des. 220 (2022), https://doi.org/10.1016/j.matdes.2022.110800 110800.

[43] X. Wang, T. Zeng, G. Xu, K. Zhang, S. Yu, Predicting the equivalent thermal conductivity of pyramidal lattice core sandwich structures based on Monte Carlo model, Int. J. Therm. Sci. 161 (2021), https://doi.org/10.1016/j.ijthermalsci.2020.106701 106701.

[44] T. Cheng, Y. Tang, L. Zhang, Update of thermodynamic descriptions of the binary Al-Sn and ternary Mg-Al-Sn systems, Calphad Comput. Coupl. Phase Diagrams Thermochem. 64 (2019) 354–363, https://doi.org/10.1016/j.calphad.2019.01.005.

[45] S. Deepak Kumar, A. Mandal, M. Chakraborty, Solid fraction evolution characteristics of semi-solid A356 alloy and in-situ A356-TiB2 composites investigated by differential thermal analysis, Int. J. Miner. Metall. Mater. 22 (2015) 389–394, https://doi.org/10.1007/s12613-015-1084-0.

[46] G.B. Schaffer, B.J. Hall, The influence of the atmosphere on the sintering of aluminum, Metall. Mater. Trans. A Phys. Metall. Mater. Sci. 33 (2002) 3279–3284, https://doi.org/10.1007/s11661-002-0314-z.

[47] L. Wang, M. Makhlouf, D. Apelian, Aluminium die casting alloys: alloy composition, microstructure, and properties-performance relationships, Int. Mater. Rev. 40 (1995) 221–238, https://doi.org/10.1179/imr.1995.40.6.221.

[48] D.R. Askeland, P.P. Fulay, W.J. Wright, The science and engineering of materials, 2010.

[49] K.S. Cruz, J.E. Spinelli, I.L. Ferreira, N. Cheung, A. Garcia, Microstructural development in Al-Sn alloys directionally solidified under transient heat flow conditions, Mater. Chem. Phys. 109 (2008) 87–98, https://doi.org/10.1016/j.matchemphys.2007.10.037.

[50] V.T. Deshpande, D.B. Sirdeshmukh, Thermal expansion of tetragonal tin, Acta Crystallogr. 14 (1961) 355–356, https://doi.org/10.1107/s0365110x61001212.

[51] F.C. Nix, D. MacNair, The thermal expansion of pure metals: Copper, Gold, Aluminum, Nickel and iron, Phys. Rev. 60 (1941) 597–605.

[52] G.K. Sigworth, T.A. Kuhn, Grain refinement in aluminum casting alloys, Int. J. Met. 1 (2007) 31–40, https://doi.org/10.1007/BF03355416.

[53] M. Colombo, E. Gariboldi, A. Morri, Er addition to Al-Si-Mg-based casting alloy: effects on microstructure, room and high temperature mechanical properties, J. Alloys Compd. 708 (2017) 1234–1244, https://doi.org/10.1016/j.jallcom.2017.03.076.

[54] G.K. Sigworth, The modification of Ai-Si casting alloys: important practical and theoretical aspects, Int. J. Met. 19–40 (2008).

[55] L. Abou-Khalil, K.S. da Cruz, G. Reinhart, N. Mangelinck-Noël, H. Nguyen-Thi, Influence of growth velocity on fragmentation during directional solidification of Al – 14 wt.% Sn alloy studied by in-situ synchrotron X-radiography, Acta Mater. 241 (2022), https://doi.org/10.1016/j.actamat.2022.118370 118370.

[56] K.T. Kashyap, T. Chandrashekar, Effects and mechanisms of grain refinement in aluminium alloys, Bull. Mater. Sci. 24 (2001) 345–353, https://doi.org/10.1007/BF02708630.

[57] I.H. Jung, D.H. Kang, W.J. Park, N.J. Kim, S.H. Ahn, Thermodynamic modeling of the Mg-Si-Sn system, Calphad Comput. Coupl. Phase Diagrams Thermochem. 31 (2007) 192–200, https://doi.org/10.1016/j.calphad.2006.12.003.

[58] H.Y. Chen, N. Savvides, Eutectic Microstructure and Thermoelectric Properties of Mg 2 Sn 39 (2010) 1792–1797, https://doi.org/10.1007/s11664-010-1150-3.

[59] D. Zhou, J. Liu, S. Xu, P. Peng, Thermal stability and elastic properties of Mg2X (X = Si, Ge, Sn, Pb) phases from first-principle calculations, Comput. Mater. Sci. 51 (2012) 409–414, https://doi.org/10.1016/j.commatsci.2011.07.012.

[60] G.N. Dul'nev, Y.P. Zarichnyak, Thermal Conductivity of liquid mixtures, Inzhenerno-Fizicheskii Zhurnal. 11 (1966) 747–750.

[61] E. Gariboldi, Z. Li, A.J. Rawson, Effective thermal conductivity in BCC and FCC lattices for all volume fractions and conductivity ratios: Analyses by microstructural efficiency and morphology factor and analytic models, Mater. Today Commun. 33 (2022), https://doi.org/10.1016/j.mtcomm.2022.104253 104253.

[62] Q.G. Wang, D. Apelian, D.A. Lados, Fatigue behavior of A356/357 aluminum cast alloys. Part II - Effect of microstructural constituents, J. Light Met. 1 (2001) 85–97, https://doi.org/10.1016/S1471-5317(00)00009-2.

[63] L. Ceschini, A. Morri, A. Morri, A. Gamberini, S. Messieri, Correlation between ultimate tensile strength and solidification microstructure for the sand cast A357 aluminium alloy, Mater. Des. 30 (2009) 4525–4531, https://doi.org/10.1016/j.matdes.2009.05.012.

[64] B.B. Straumal, W. Gust, D.A. Molodov, Wetting transition on grain boundaries in Al contacting with a Sn-rich melt, Interface Sci. 3 (1995) 127–132, https://doi.org/10.1007/BF00207014.

[65] C. Confalonieri, P. Bassani, E. Gariboldi, Microstructural and thermal response evolution of metallic form-stable phase change materials produced from ball-milled powders, J. Therm. Anal. Calorim. 142 (2020) 85–96, https://doi.org/10.1007/s10973-020-09785-7.

[66] W. Kim, K. Jang, K. Ji, C. Lee, Effects of heat treatment on the microstructure and hardness of a356 (Alsi7 mg0.3) manufactured by vertical centrifugal casting, Appl. Sci. 11 (2021), https://doi.org/10.3390/app112311572.

[67] P. Bassani, E. Gariboldi, G. Vimercati, Calorimetric analyses on aged Al-4.4Cu-0.5Mg-0.9Si-0.8Mn alloy (AA2014 grade), J. Therm. Anal. Calorim. 87 (2007) 247–253, https://doi.org/10.1007/s10973-006-7836-3.

[68] P. Bassani, E. Gariboldi, A. Tuissi, Calorimetric analysis of AM60 magnesium alloy, J. Therm. Anal. Calorim. 80 (2005) 739–747, https://doi.org/10.1007/s10973-005-0723-5.

[69] P.J. Shamberger, N.M. Bruno, Review of metallic phase change materials for high heat flux transient thermal management applications, Appl. Energy. 258 (2020), https://doi.org/10.1016/j.apenergy.2019.113955 113955.

[70] J. Nieto-Maestre, I. Iparraguirre-Torres, Z.A. Velasco, I. Kaltzakorta, M.M. Zubieta, Novel metallic alloys as phase change materials for heat storage in direct steam generation applications, AIP Conf. Proc. 1734 (2016), https://doi.org/10.1063/1.4949130.

[71] C. Confalonieri, E. Boller, Y. Cheng, E. Gariboldi, Synchrotron radiation micro-CT with phase contrast for high-temperature in-situ microstructural characterization of Al[sbnd]Sn composite phase change materials, Mater. Charact. 193 (2022), https://doi.org/10.1016/j.matchar.2022.112302 112302.